Role of Polytetrahedral Structures in the Elongation and Rupture of Gold Nanowires

Christopher R. Iacovella,[†] William R. French,[†] Brandon G. Cook,[‡] Paul R. C. Kent,[§] and Peter T. Cummings[†,§,*]

[†]Department of Chemical and Biomolecular Engineering and [‡]Department of Physics and Astronomy, Vanderbilt University, Nashville, Tennessee 37235-1604, United States and, [§]Center for Nanophase Materials Sciences, Oak Ridge National Laboratory, Oak Ridge, Tennessee 37831-6494, United States

ABSTRACT We report comprehensive high-accuracy molecular dynamics simulations using the ReaxFF force field to explore the structural changes that occur as Au nanowires are elongated, establishing trends as a function of both temperature and nanowire diameter. Our simulations and subsequent quantitative structural analysis reveal that polytetrahedral structures (*e.g.*, icosahedra) form within the "amorphous" neck regions, most prominently for systems with small diameter at high temperature. We demonstrate that the formation of polytetrahedra diminishes the conductance quantization as compared to systems without this structural motif. We demonstrate that use of the ReaxFF force field, fitted to high-accuracy first-principles calculations of Au, combines the accuracy of quantum calculations with the speed of semiempirical methods.

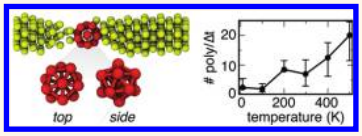

KEYWORDS: gold, nanowire · atomic-scale contacts · polytetrahedra · icosahedra · electron-transport · conductance · simulation · density functional theory · molecular dynamics · reactive force fields

The observation of conductance quantization in atomic-scale junctions[1−5] has fueled much interest in understanding their formation in mechanically deformed metallic nanowires (NWs),[6−17] in large part due to potential applications in nano- and molecular electronic devices. To this extent, quantifying the structural changes that occur as a NW elongates is important for understanding how and why parameters such as initial crystal structure,[7,8] temperature,[14] and rate of elongation[11,14] affect the material properties, such as conductance,[18−21] mechanical stability,[11,22] or the opening of a band gap.[23] Many studies have been performed that focus on identifying changes to the crystalline structure, such as slipping and reorientation of the crystalline lattice,[6,13,14,17,24] and under what conditions single-atom-wide monatomic chains are likely to form.[3,4,7,14,17] However, to date, there has only been limited emphasis on quantifying the formation and structure of the "amorphous" or, more generally, noncrystalline domains that often appear within NWs.[13,18,21,25] The formation of these noncrystalline structures is likely to result in significant changes to the properties of the NWs. For example, amorphous structures separating otherwise crystalline NW domains may exhibit unique dynamical properties akin to glass-forming liquids, similar to atoms at grain boundaries in bulk metals.[26] Moreover, noncrystalline structures may still demonstrate distinct local ordering, such as the distorted icosahedral structures predicted to form in the necks of Na NWs[18] and the recent synthesis of bimetallic NWs with local icosahedral ordering.[27] This is of particular consequence as thiolated icosahedral Au NWs are predicted to behave as semiconductors under certain charge states[28] and noncrystalline NW neck structures have recently been demonstrated to produce gradual changes in the conductance, as opposed the more typical quantization (*i.e.*, "steps" and "plateaus").[21]

In this paper, we focus on identifying the amorphous/noncrystalline structures that form within simulated Au NWs undergoing tensile elongation. Simulation is well suited to study this problem as it provides the full spatial and temporal coordinates of the atoms in the NW, allowing the structure to be quantified by the use of order parameters, such as those recently adapted from the field of shape matching.[29−31] Much of the previous simulation work dealing with the elongation of Au NWs has relied on either quantum mechanical[8,12,17,21,32−34] or, more commonly, semiempirical methods,[7,9,10,12,14,22,24,35,36] requiring a compromise between the accuracy of the interatomic interactions and the accessible system size and time scale. Quantum mechanical methods, such as density functional theory (DFT), are widely considered to provide a highly accurate description of the interactions between Au atoms, in

* Address correspondence to peter.cummings@vanderbilt.edu.

Received for review October 12, 2011 and accepted October 31, 2011.

Published online October 31, 2011
10.1021/nn203941r

© 2011 American Chemical Society

particular, capturing the stability of 2-D planar geometries for low coordination clusters.[37,38] However, the high computational cost of quantum mechanical methods often limits both the total number of independent statepoints that can be efficiently considered and the total size of the NW, typically ~100 atoms or less,[17,33] both of which may inadvertently bias the results. Semiempirical methods, such as the second-moment approximation of the tight-binding (TB-SMA) scheme,[39] are many orders of magnitude faster than quantum mechanical methods, allowing for the efficient exploration of large numbers of statepoints and systems sizes more representative of experiment.[7,10,12,14] While methods such as TB-SMA have been shown to qualitatively match the behavior of experiment in side-by-side studies,[7] semiempirical methods are often fitted to bulk systems and thus may produce results that are quantitatively inconsistent with theory or experiment,[40] especially for low coordination atomic-scale contacts.[38,41] In particular, the minimal energy 2-D planar structures of Au are not typically stable for semiempirical methods,[38] which may incorrectly bias NW simulations toward forming 3-D isomers.

In order to bridge the gap between semiempirical and quantum mechanical methods, we use the ReaxFF reactive force field,[42] which is designed to provide accuracy approaching quantum mechanical methods but at a substantially reduced computational cost. ReaxFF force fields are derived by fitting analytical functions to DFT bonding curves.[38,42] The parameters derived for Au by Keith *et al.*[38] have been demonstrated to satisfactorily capture the expected behavior of both bulk and low coordination states.[38] In particular, this parametrization has been shown to closely reproduce the energy and stability of low and minimal energy clusters of Au.[38] In this work, we show that ReaxFF is a substantial improvement over TB-SMA for the simulation of NW structures by comparing the absolute and relative energy scaling to DFT calculations. We perform comprehensive molecular dynamics (MD) simulations[43] with ReaxFF to investigate the behavior and properties of [100]-oriented face-centered cubic (fcc) Au NWs undergoing tensile elongation in vacuum, which we also compare to simulations performed using TB-SMA. We report, for the first time, the formation of well-ordered polytetrahedral local structures (*e.g.*, full and partially coordinated icosahedra[44]) within the noncrystalline domains of the NWs. We quantify the formation of these structures by using the R_{ylm} shape matching method[29−31,45] based on spherical harmonics,[46] which we use to construct trends as a function of temperature and NW diameter. We further calculate the zero-bias conductance of our simulation trajectories to demonstrate the impact that the formation of polytetrahedra has on the conductance behavior.

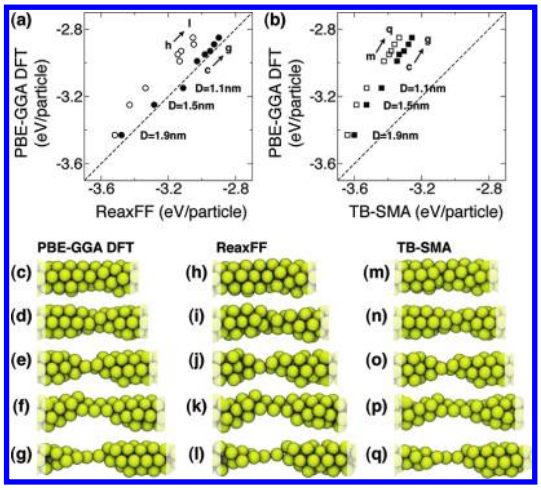

Figure 1. (a) DFT energy *vs* ReaxFF energy. (b) DFT energy *vs* TB-SMA energy. (a,b) Filled symbols correspond to the energy calculated of structures that have been energy-minimized with DFT, open symbols correspond to energy of structures energy-minimized with each of the methods (*e.g.*, DFT energy-minimized and ReaxFF energy-minimized). Snapshots of the energy-minimized configurations of the elongation sequence for (c−g) DFT, (h−l) ReaxFF, and (m−q) TB-SMA.

RESULTS

Validation of ReaxFF for Au NWs. We first assess the energetic description of Au NWs predicted by ReaxFF by comparing to DFT and TB-SMA. We report the energy for [100]-oriented periodic fcc NWs with diameters, $D = 1.1$, 1.5, and 1.9 nm, as well as an elongation sequence of a periodic 0.85 nm NW. The elongation sequence is representative of the low coordination structures typically found in the necks of mechanically deformed NWs. We perform DFT calculations that make use the generalized gradient approximation by Perdew, Burke, and Ernzerhof (PBE-GGA) and additionally include spin−orbital coupling (see Methods). All reported DFT energy values are calculated using structures that have been fully and self-consistently energy-minimized.

In Figure 1a, we plot the energy calculated with DFT *versus* the energy calculated with ReaxFF. In this plotting scheme, an ideal match between DFT and ReaxFF occurs if the data point falls along the line $y = x$. In Figure 1a, filled symbols represent the energy calculated using the coordinates energy-minimized with DFT (*i.e.*, when calculating the ReaxFF energy, atoms are static and arranged according to the configuration generated with DFT). The DFT energy-minimized configurations for the elongation sequence are shown in Figure 1c−g. We observe that ReaxFF is capable of accurately reproducing the per particle energy predicted by DFT, where the magnitude of the difference is less than 0.05 eV per atom and all data points fall along the line $y = x$. In Figure 1a, data points with open symbols correspond to energy-minimized structures predicted by the two different treatments (*i.e.*, the DFT

energy corresponds to the structure energy-minimized with DFT, and the ReaxFF energy corresponds to the structure energy-minimized with ReaxFF). The ReaxFF structures are generated starting from the DFT-optimized structures. The energy-minimized elongation sequence for ReaxFF is shown in Figure 1h–l, where we observe minor changes as compared to the DFT structures in Figure 1c–g. Note, the preferred interatomic spacings will vary slightly between methods, thus we use a two-stage energy minimization for ReaxFF, first allowing the box volume to change to minimize pressure (which scales atom positions), then allowing atom positions to change in order to minimize the potential energy. For minimized configurations, ReaxFF predicts a lower energy structure than DFT for all statepoints. However, the values are still close, where the magnitude of the deviation varies from 0.09 to 0.20 eV/particle; for comparison, previous PBE-GGA DFT calculations of bulk Au have been reported to deviate by 0.08 eV/atom when compared to experiment (*e.g.*, $E_{\mathrm{ReaxFF}} = -3.85$ eV/atom[38] and $E_{\mathrm{exp}} = -3.93$ eV/atom[47]).

Figure 1b is constructed in the same manner as Figure 1a but using TB-SMA rather than ReaxFF. Again, filled symbols represent the energy calculated using the DFT energy-minimized structures. TB-SMA fails to closely reproduce the energy, predicting lower values than DFT for all structures. Here the magnitude of the differences ranges from 0.17 to 0.41 eV/atom. Open symbols again represent the energy of structures minimized with the two methods. We use a similar procedure for TB-SMA as we did for ReaxFF. The energy-minimized structures of TB-SMA are shown in Figure 1m–q, where we observe only minor differences when compared to either DFT or ReaxFF structures. The most noticeable difference is observed in Figure 1q, where the left-hand side of the NW compresses into a more locally dense state. For energy-minimized structures, the energy predicted by TB-SMA is shifted to even more negative values, where now the magnitude of the energy difference with DFT ranges from 0.21 to 0.47 eV/atom.

In addition to comparing the absolute energy, we examine the relative change in energy ranging from the highest coordination state ($D = 1.9$ nm NW) to the lowest coordination state (*i.e.*, the final elongated structure, shown in Figure 1g,l,q). This can be assessed by examining the slope of the data points shown in Figure 1a,b; a slope of unity provides an ideal energy change with respect to DFT. For the ReaxFF calculations in Figure 1a, we observe a slope of 0.99 for the static structure (filled symbols) and 1.11 for the energy-minimized structures (open symbols) using linear regression. Thus, even though the absolute energies are slightly different for the energy-minimized states (open symbols), the relative change predicted by ReaxFF is in very good agreement with DFT. For the TB-SMA calculations in Figure 1b, we observe a slope of 1.63 for static calculations (filled symbols) and a slope of 1.81 for energy-minimized structures (open symbols). The strong deviation from unity indicates that TB-SMA fails to properly predict the energy loss associated with a reduction in average coordination number, which may strongly influence the structural evolution of the NW.

In previous work comparing common semiempirical methods for the elongation of finite Au NWs, TB-SMA was demonstrated to provide the best agreement with DFT in terms of the relative energy change.[12] Thus it appears that ReaxFF is an improvement over TB-SMA, providing a better description of both the relative energy change and absolute energy for Au NWs. This improvement results from the increased sophistication of the form of the ReaxFF force field relative to TB-SMA,[38,39] which enables ReaxFF to better account for a reduction in atomic coordination. Additionally, the ReaxFF parameters are derived for a host of conditions, including atoms forming dimers, at surfaces, and in the bulk;[38] TB-SMA is parametrized only for the bulk.[39] We note that the parameters of Keith *et al.* were not derived specifically to match NW properties; incorporation of NW data into the training set might further improve the accuracy of ReaxFF for this application, reducing the deviation between ReaxFF and DFT when comparing energy-minimized structures.

Formation of Polytetrahedral Structures. We perform simulations of cylindrical Au NWs of length 3.6 nm, with diameters, $D = 1.1$, 1.5, and 1.9 nm (177, 317, and 589 atoms, respectively) for a variety of statepoints, calculating 10 independent simulations for each parameter combination (see Methods for more details). Here we focus on ReaxFF-based simulations but also include TB-SMA-based simulations for comparison. In these ReaxFF simulations, we observe that, as a typical Au NW elongates, a small region begins to "neck", becoming narrower than the original diameter. The neck forms in response to the applied tensile load, localizing many of the structural changes to this neck region, allowing the bulk of the NW to relax its configuration. Within the necks of our simulated NWs, we often observe the formation of noncrystalline structures with distinct ring- and crescent-like geometries. Figure 2a shows a representative ReaxFF simulation snapshot of a $D = 1.1$ nm NW at $T = 298$ K, shortly after neck formation; an individual ring-like structure is highlighted in the snapshot with an enlarged version, extracted from the system, shown to the right. Figure 2b shows a representative snapshot of a $D = 1.5$ nm NW where two crescent-like structures are highlighted and extracted. These ring- and crescent-like structures are polytetrahedral in nature, where the local structure of the atoms can be decomposed solely into individual tetrahedral subunits.[44] Specifically, the highlighted structure in Figure 2a is best classified as

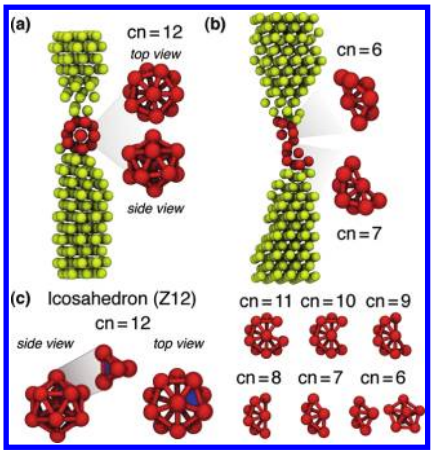

Figure 2. Representative ReaxFF simulation snapshots of NWs at $T = 298$ K elongated at 0.1 m/s for (a) $D = 1.1$ nm NW elongated by 12.2 Å and (b) $D = 1.5$ nm NW elongated by 21.9 Å. (a,b) Atoms are rendered at ~75% of their true size with individual polytetrahedral structures highlighted within the NW and shown at the right. (c) Rendering of a Z12 structure, *i.e.*, an icosahedron, with an individual tetrahedral subunit highlighted. Partial Z12 clusters are shown as a function of coordination number, cn, varying from fully coordinated, cn = 12, to cn = 6. Note, cn = 6 shows two different partial clusters commonly observed.

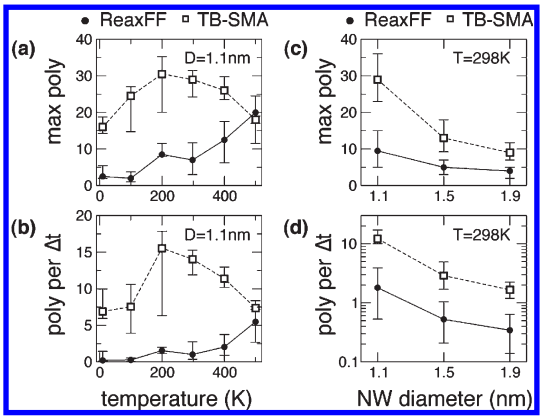

Figure 3. Quantification of polytetrahedral structures. (a) Maximum number of polytetrahedral clusters observed concurrently in a trajectory and (b) number of polytetrahedra per time step, both for $D = 1.1$ nm and shown as a function of temperature for NWs pulled at 1 m/s, calculated from 120 total independent simulations. (c) Maximum number of polytetrahedral clusters observed concurrently in a trajectory and (d) number of polytetrahedra per time step, both at $T = 298$ K and shown as a function of diameter, calculated from 400 total independent simulations. Data for (c,d) are presented as the aggregate of simulations conducted from 0.1 to 5 m/s, as a strong rate dependence was not observed. All data points correspond to the median, and error bars correspond to first and third quartiles. The legends shown at the top are applicable to all plots.

an icosahedron. An icosahedron is constructed of 13 particles arranged as two splayed pentagonal pyramids (composed of 20 total tetrahedral subunits), demonstrating five-fold symmetry;[44] an ideal icosahedron is shown in Figure 2c. The two highlighted clusters in Figure 2b are partially coordinated icosahedral clusters that maintain the same basic geometry of the full cluster but with X number of particles removed (*i.e.*, several tetrahedral subunits removed).[29] Ideal partial clusters of various coordination are shown in Figure 2c. TB-SMA simulations also demonstrate polytetrahedral structures within the necks of the elongated NWs, similar to Figure 2a,b.

To quantify the structures formed in our simulations and establish trends, we use the R_{ylm} method to determine which atoms are in polytetrahedral local environments (see Methods). We use this quantitative information to construct three metrics: (1) the maximum number of polytetrahedra that occur concurrently during the course of a simulation trajectory, (2) the number of polytetrahedra per time step in a simulation (calculated by normalizing the total number of polytetrahedra observed by the total number of statepoints considered), and (3) the coordination number (cn) histogram of polytetrahedral atoms.

We first report the behavior of thin NWs with $D = 1.1$ nm elongated at a rate of 1 m/s for $T = \{10, 100, 200, 298, 400, 500\}$ K. Figure 3a,b plots the maximum number of polytetrahedra and the polytetrahedra per time step, respectively. In all cases, we report median values, where error bars correspond to the first and third quartiles, since the data are not necessarily well described by a Gaussian distribution. ReaxFF simulations demonstrate a steady increase in both metrics as temperature is increased; that is, both the maximum size of the polytetrahedral domains and the likelihood of finding polytetrahedra increases as T increases. The polytetrahedral motif is not prominent for ReaxFF systems at low temperature (*i.e.*, $T < 200$ K). While the behavior of the ReaxFF and TB-SMA potentials converge for high temperature, TB-SMA demonstrates markedly different trends and behavior. Overall, we observe that TB-SMA predicts a significantly larger value of both the maximum number of polytetrahedra and polytetrahedra per time step than the ReaxFF simulations. TB-SMA predicts two regimes with an approximate crossover of $T = 200$ K. TB-SMA systems at $T = 10$ and 100 K tend to maintain a predominantly fcc structure, whereas higher temperature states transition into A3 core–shell helical structures[48] upon moderate amounts of elongation. For example, at $T = 298$ K, 70% of the TB-SMA simulations transform into predominantly A3 structured NWs by the time the NW has been elongated by 5 Å. The A3 structure is locally composed of tetrahedral subunits that closely match the polytetrahedral structures in our R_{ylm} reference library. However, we note that even for $T < 200$ K, where A3 structures are not found with either potential, ReaxFF still forms fewer polytetrahedra than TB-SMA, by a factor of ~10 for both metrics. The predominance of crystalline structures at low temperature predicted by ReaxFF is more consistent with results of zero temperature DFT calculations performed for the elongation of [110] and [111] Au NWs.[17,21]

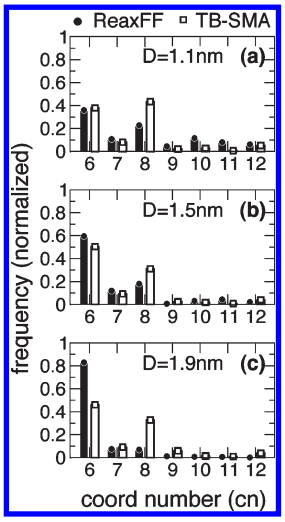

Figure 4. Histograms of the coordination number (cn) of polytetrahedral structures for NWs with (a) $D = 1.1$ nm, (b) $D = 1.5$ nm, and (c) $D = 1.9$ nm. All data are at $T = 298$ K and are presented as the aggregate of simulations conducted from 0.1 to 5 m/s. The legend at the top is applicable to all plots.

Figure 3c,d plots the median value of the maximum number of polytetrahedra and polytetrahedra per time step, respectively, for NWs as a function of NW diameter; these simulations are performed at $T = 298$ K, as this statepoint demonstrates, appreciable numbers of polytetrahedra for both potentials and temperatures in this vicinity are common in experiment.[6,7] The values reported in Figure 3c,d correspond to the aggregate of simulations performed for rates 0.1 to 5 m/s, as we did not observe strong variability with rate of elongation. We observe that the median value of both metrics decreases with increasing diameter for both ReaxFF and TB-SMA. That is, the likelihood of forming polytetrahedra decreases with increasing NW diameter. In all cases, ReaxFF-based simulations predict smaller median values for the two metrics than TB-SMA, with the largest differences occurring for the $D = 1.1$ nm NWs. The differences we observe between ReaxFF and TB-SMA are likely related to the energy scaling we previously explored, where TB-SMA overpredicts both the absolute magnitude and relative energy of lower coordination states.

Figure 4 plots histograms of the coordination number of atoms identified as having polytetrahedral local ordering for NWs at $T = 298$ K (corresponding to the data presented in Figure 3c,d). Histograms of ReaxFF simulations demonstrate a diameter dependence; $D = 1.1$ nm NWs show two key peaks at cn = 6 and 8, but the relative fraction of cn = 6 strongly increases with increasing diameter. For $D = 1.9$ nm NWs simulated with ReaxFF, ~80% of the observed polytetrahedral clusters have cn = 6. Histograms generated from TB-SMA simulations demonstrate two clear peaks at cn = 6 and 8, encompassing ~80% of the total polytetrahedral structures, with much less dependence on diameter.

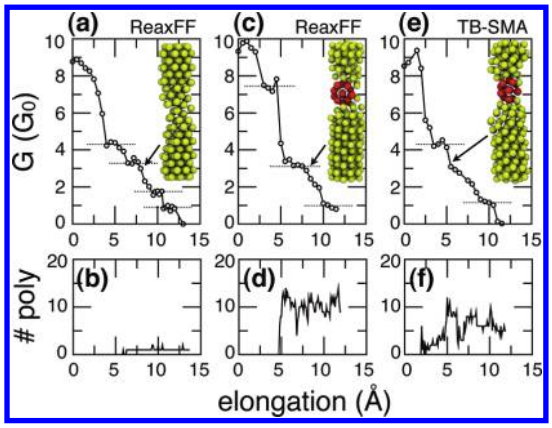

Figure 5. (a) Conductance and (b) number of polytetrahedra as a function of elongation of a ReaxFF NW at $T = 298$ K. (c) Conductance and (d) number of polytetrahedra of a ReaxFF NW at $T = 10$ K. (e) Conductance and (f) number of polytetrahedra of a TB-SMA NW at $T = 10$ K. All data correspond to NWs with $D = 1.1$ nm elongated at 1 m/s. Plateaus are highlighted with horizontal dotted lines. Simulation snapshots for configurations with $G \sim 3G_0$ are shown in the inset in each figure, where c and e each highlight a polytetrahedral structure in the neck (red).

Zero-Bias Conductance. We calculate the zero-bias conductance of several representative trajectories generated with ReaxFF and TB-SMA in order to assess the impact of polytetrahedra; that is, is there a characteristic conductance "fingerprint" associated with their formation. As described in the Methods section, we use a combined DFT-non-equilibrium Green's function technique to calculate the conductance,[49] which we report in terms of $G_0 = 2e^2/h$, where e is the charge of an electron and h is Planck's constant. In experiment, a typical conductance trace demonstrates a "staircase" behavior, with abrupt plateaus and drops as a function of elongation. The abrupt changes in the conductance coincide with structural rearrangements of the atoms, such as thinning of the NW neck. For very small cross sections, the steps often occur at roughly integer multiples (m) of G_0. It is important to note that histograms of conductance tend to demonstrate a substantial spread around each of these integer peaks,[50] and as a result, non-integer values are also regularly observed in experiment. Recent work has correlated the formation of non-integer plateaus to the difference in dimensionality of the local structures within the NW neck (*i.e.*, the difference between three-, two-, and one-dimensional atomic arrangements).[21]

Figure 5 plots the conductance and number of polytetrahedra as a function of elongation for trajectories of $D = 1.1$ nm NWs elongated at 1 m/s, generated with both ReaxFF and TB-SMA. We first consider a ReaxFF trajectory at $T = 298$ K that does not demonstrate any significant polytetrahedral ordering, as shown in Figures 5a,b. We observe distinct stepwise behavior with conductance plateaus at roughly integer multiples of G_0 ($m \sim 1, 2, 3$, and $4G_0$, highlighted in Figure 5a with horizontal lines). Additionally, the length of these plateaus ranges from 1.5 to 3.5 Å, which matches the approximate plateau length of 1−4 Å seen in experiments at $T = 4$ K[4] and

$T = 298$ K.[6] A snapshot of the NW at $\sim 3G_0$ in the inset of Figure 5a shows a crystalline neck structure.

Figure 5c,d plots data for a NW trajectory generated with ReaxFF at $T = 10$ K. As before, we observe stepwise behavior in the conductance. In contrast to the previous trajectory, we now observe the formation of an appreciable number of polytetrahedral structures, as shown in Figure 5d. The formation of polytetrahedra appears to have a distinct impact on the conductance. For example, while we observe plateaus at $m \sim 3$ and $1G_0$ in Figure 5c, there is a gradual change in conductance between these two steps rather than a plateau at $2G_0$. The onset of the formation of polytetrahedral structures at ~5 Å correlates with the start of the conductance plateau at $3G_0$. Visually, we observe that at the start of the gradual change (*i.e.*, $3G_0$), the narrowest region of the neck is spanned by a polytetrahedral structure ~3 atoms wide; a shapshot is shown in the inset of Figure 5c.

We further assess the impact of polytetrahedra by examining a trajectory at $T = 10$ K generated with TB-SMA, as shown in Figure 5e,f. Recall that TB-SMA overpredicts the tendency to form polytetrahedra as compared to ReaxFF, making it ideal for assessing their impact. We still observe step-like behavior but now only see plateaus at $m \sim 4$ and $1G_0$. Again, we observe a rather gradual transition, here from $4G_0$ to $1G_0$. While the onset of polytetrahedra appears at 2.5 Å of elongation, the most significant peak occurs at ~5 Å (see Figure 5f), which correlates to the start of the gradual change in conductance. As was noted in Figure 5c, we also observe that at $\sim 3G_0$ (*i.e.*, the start of the gradual change), the narrowest region of the neck is spanned by a polytetrahedral structure ~3 atom diameters across (a shapshot is shown in the inset of Figure 5c). Thus, it appears that the gradual conductance changes we observe are associated with the formation of polytetrahedra that span the cross section of the neck. This is likely related to different modes of mechanical deformation exhibited by tetrahedral structures *versus* crystals; the mechanical behavior of related core–shell NWs as compared to crystals has previously been explored in ref 9.

Our results regarding the impact of polytetrahedral neck structures on the conductance are supported by recent simulations of Tavazza *et al.* that used DFT to investigate the elongation of [110] and [111] Au NWs at zero temperature.[21] In that work, nearly identical conductance behavior was observed for systems that demonstrated noncrystalline neck structures, that is, gradual changes from $3G_0$ to $1G_0$.[21] Similar conductance traces were also observed in experiments at $T = 4$ K.[21] Additionally, it was noted that systems exhibiting this gradual conductance change occurred in the minority of simulations and experiments, suggesting that noncrystalline structures are rare at these very low temperatures.[21] As shown in Figure 2a,b, our ReaxFF simulations also predict that the noncrystalline polytetrahedral structures are a rare structural motif at low temperature.

DISCUSSION

The formation of polytetrahedral structures within the necks of the elongated Au NWs may be surprising as icosahedra are not predicted to be the lowest energy structures.[51–53] Generally speaking, planar structures are predicted to be the minimal energy states for small, isolated clusters of Au.[37,51] However, this does not imply that icosahedra, or other low, but not minimal energy, structures are inherently unstable. To assess the stability of the polytetrahedral structures, we perform conjugate gradient energy minimization using DFT of the isolated icosahedral clusters shown in Figure 2c. Starting from both ideal structures and those generated with ReaxFF, we find that clusters with cn = 6, 8, 9, and 12 maintain their original geometry at the end of the minimization, suggesting that these structures are locally stable. We also note that systems that start as partial icosahedra with cn = 10 and 11 relax their structures into more "flattened" states that, in 3 out of 4 calculations, contain a distinct polytetrahedral pentagonal dipyramind (*i.e.*, a cn = 6 polytetrahedral structure). Recall that the cn = 6 structure is the most common polytetrahedral configuration found in our simulations. Furthermore, polytetrahedral structures of Au are well reported in experiment and theory, including monolayer-protected icosahedral clusters with cn = 12,[54] phosphone-thiolate-protected partial polytetrahedral Au structures,[55] and bi-icosahedral clusters of both face-sharing[56] and vertex-sharing icosahedra.[57]

The polytetrahedral structures we observe in our simulations are not isolated clusters, but rather occur within the context of a larger, mechanically deformed NW. The average coordination number of atoms in an isolated cluster will be lower than an equivalent configuration that occurs within a NW. Additionally, we must also consider that these structures form as a result of mechanically deforming a NW *via* an applied tensile load. Previous experiments of NWs pulled at a constant rate demonstrate a sawtooth-like behavior in the mechanical force on the NW as a function of elongation,[58] and thus the local forces of the atoms may be far from equilibrium and constantly changing. The original structure of the NW will also dictate how it can respond to tensile loads.[7,9] For example, it has been demonstrated that the likelihood of forming monatomic Au chains in elongated Au NWs is influenced by the original orientation of the crystalline lattice (*i.e.*, [111] *vs* [110] *vs* [100]).[7] Focusing only on minimal potential energy structural motifs also ignores the importance of thermal effects. Recall that in Figure 3a, b we observed that the formation of polytetrahedral structures is very unlikely at low temperature but increases with temperature. Previous work from our group proposed a universal energy release mechanism that outlines the strong role that temperature and rate of elongation can play in determining how a NW responds to the applied tensile load.[14]

Additionally, Au is ductile, which manifests itself as a tendency for the NW to remain in a cylindrical, connected structure by thinning within the neck region. As the neck of the NW thins, polytetrahedral structures may become the optimal configurations since they are able to span narrow, cylindrical-like geometries by forming face-sharing polytetrahedral helices[28,59,60] or vertex-sharing structures.[28,57] This was demonstrated for particles with van der Waals interactions, where a transition was observed from fcc/hcp (hexagonal close-packed) structures to polytetrahedral structures upon decreasing the diameter of the confining cylinder.[29] Similar behavior was also demonstrated for Au, where tetrahedral helices were predicted to be the optimal structures for small diameter NWs whereas fcc structures were optimal for large diameter NWs.[48] Recent experimental work has demonstrated the synthesis of thin Au/Ag NWs that are locally constructed of face-sharing icosahedra,[27] additionally demonstrating this packing motif for metallic NWs. Furthermore, the formation of polytetrahedral structures within the necks of elongating NWs is not without precedent. Previous DFT calculations of the mechanical deformation of [100]-oriented (body-centered cubic) bcc Na NWs demonstrated the formation of distorted full and partial icosahedra within the NW neck.[18] This may suggest that the formation of polytetrahedra is a universal relaxation mechanism for mechanically deformed NWs.

The formation of polytetrahedral structures may have important implications regarding the electronic properties of the NW. As we saw in Figure 5, the formation of polytetrahedra diminishes the quantization of the conductance traces. Combined with the increased likelihood of forming polytetrahedra as temperature increases, this may be important to consider when engineering nanoelectronic devices designed to operate at, for example, room temperature. The impact of polytetrahedra may be even more substantial. The work of Jiang *et al.* predicts that thiolated vertex-sharing icosahedral Au NWs behave as a semiconductor for the -2 and $+2$ charge states.[28] This suggest that Au NWs elongated in the presence of a thiol solvent might, under certain conditions, change from behaving as metals to semiconductors as a result of the formation of polytetrahedral neck structures.

However, it is important to note that in the current study we only explore relatively short NWs (3.6 nm long) with rigidly fixed ends, elongated at high rates. While our strain rates ($\sim 10^7 - 10^8$ s^{-1}) are similar to typical rates reported in prior simulations[24] and good agreement is seen between simulation and experiment,[7,21] it is known that the strain rate in simulation is significantly higher than in typical experiments.[24] It has been demonstrated that, under certain conditions, the intermediate structural motifs in NWs are significantly impacted by the strain rate[14,17,24] and the formation of amorphous domains becomes more likely as strain rate increases.[25] Therefore, even though we did not observe strong trends with respect to the rate of elongation—and hence strain rate—at the state-points considered here (*i.e.*, rates = 0.1 to 5 m/s at T = 298 K), the likelihood of forming amorphous domains (*i.e.*, polytetrahedra) may be enhanced in our simulations as compared to experiment due to the very high strain rates. Thus, investigations of the formation of polytetrahedra at significantly reduced strain rates is an important direction for future study.

CONCLUSION

In this work, we showed good agreement between ReaxFF and DFT in terms of the absolute energy and relative energy scaling. We also showed that ReaxFF provides a better energetic description than the semi-empirical TB-SMA potential, which has commonly been used to study Au NW elongation. We further demonstrated the formation of polytetrahedral local structures within the necks of elongated Au NWs simulated with ReaxFF. We observed that the formation polytetrahedra is not a strong motif of structural relaxation for low temperature systems, but the likelihood of forming polytetrahedra increases with temperature. We also found that the likelihood of forming polytetrahedra increases as NW diameter decreases. Polytetrahedral order was also observed for simulations performed with the TB-SMA potential; however, TB-SMA appears to significantly overpredict their formation as compared to ReaxFF, especially for small diameter NWs and low temperature. We find that ReaxFF-based simulations produce trajectories that demonstrate clear stepwise behavior in conductance that closely matches experiment. We also observe that the formation of polytetrahedra (*i.e.*, noncrystalline structures) within the NW necks dampens the quantization behavior of the conductance, closely matching the observations in ref 21. The results presented here suggest that the formation of polytetrahedral structures within the necks of the [100]-oriented Au NWs is a ubiquitous and important mechanism for relieving the internal stress brought about by elongation, in particular, for small diameter NWs at high temperature.

METHODS

DFT Calculations. We perform DFT calculations using the generalized gradient approximation of Perdew, Burke, and Ernzerhof (PBE-GGA)[62] within the plane-wave projector-augmented wave formalism (PAW).[63,64] Our calculations were performed at the gamma point with a 230 eV plane-wave energy cutoff. The PAW potentials included the outermost d and s electrons in the valence, giving 11 electrons per atom. Significantly, we fully included spin−orbit coupling in all of our calculations of the energy and forces. All reported DFT energy

values are calculated using structures that have been fully and self-consistently energy-minimized.

Simulation Methodology. Our basic simulation procedure closely mimics the "stretch and relax" procedure of Pu *et al.*:[14] we rigidly fix the last two rows of each end of the NW creating "grip" atoms at each end; we allow the core of the system to relax for 100 ps; after relaxation, we elongate the NW by displacing the grip atoms at one end by increments of 0.05 Å, allowing the system to relax for a prescribed time between displacements, repeating until the NW breaks. We explore elongation rates from 5 m/s (1 ps relaxation between displacements) to 0.1 m/s (50 ps). This range encompasses typical elongation rates used to draw metallic whiskers with STM or AFM.[58] Simulations are conducted between T = 10 and 500 K; common experimental conditions are T = 4−10 K[4,58] and $T \sim$ 300 K.[6,7] For each statepoint, we perform 10 independent simulations to obtain sufficient statistics.

ReaxFF simulations use the fitting parameters derived by Keith *et al.*[38] This particular fitting was chosen because it was parametrized using PBE-GGA DFT, which is well suited for systems with surfaces (*i.e.*, NWs), and the elastic moduli of the fitting closely match experiment.[38] TB-SMA simulations are performed using fitting parameters derived by Cleri and Rosato.[39] TB-SMA is used as previous comparisons with DFT showed it provides a better match in terms of relative energy change than other common semiempirical potentials.[12] Both ReaxFF and TB-SMA simulations are performed using the LAMMPS simulation package[43] (extended to incorporate TB-SMA) with the Nose-Hoover thermostat for systems without periodic boundary effects. As is common, TB-SMA simulations use a time step of 2 fs,[7,10,12,14] whereas a smaller time step of 0.5 fs is needed for ReaxFF. To simulate the same time scale, ReaxFF requires more walltime than TB-SMA, by a factor of ∼50.

R_{ylm} Method. To analyze the local configurations of atoms, we employ techniques borrowed from the field of *shape matching*.[30,31] We use the R_{ylm} scheme proposed in refs 29 and 45, which allows us to objectively identify structural trends in an automated fashion. This method relies on creating a rotationally invariant spherical harmonics[46] "fingerprint" of the first neighbor shell surrounding each atom. We compare the fingerprint of each local cluster to a library of reference configurations and determine the best match. Here, we quantify the match, M, using the Euclidian distance, normalized such that it spans from 0 (worst match) to 1 (perfect match). By definition, every cluster in this scheme has a "best match" even if that match is poor. To avoid misidentification, we define a cutoff such that we ignore matches where $M < 0.86$. This provides results consistent with visual inspection; the choice of cutoff will impact the specific calculated values; however, the overall trends are not strongly perturbed by this choice.[30] Our reference library includes full and partially coordinated clusters of type fcc, hcp, and icosahedra, incorporating both ideal configurations and configurations relaxed using the ReaxFF and TB-SMA potentials, where we only consider clusters of $6 \leq cn \leq 12$.

Conductance Measurement. Conductance calculations are carried out in a combined DFT/non-equilibrium Green's function framework. A double-ζ numerical atomic orbital basis set is used (18 basis functions per Au atom) in the calculations. The zero-bias conductance is given by $G = T(E_F)$, where $T(E)$ is the transmission coefficient of the device and E_F is the Fermi energy. G is reported in units of $G_0 = 2e^2/h$, where e is the charge of an electron and h is Planck's constant. We validated our conductance measurements by investigating single-point atom contacts, finding good agreement with previous theoretical calculations.[20,21,34] Further details of the implementation and its accuracy can be found in ref 49.

Acknowledgment. This work was funded by the U.S. Department of Energy (DOE) and supported by computational resources provided by the National Energy Research Scientific Computing Center (NERSC) of the DOE under Contract No. DE-AC02-05CH11231 and the National Institute for Computational Sciences, Project-ID UT-TNEDU014.[61] W.R.F. was supported under the U.S. Department of Education Graduate Assistance in Areas of National Need (GAANN) Fellowship under Grant No. P200A090323. Research by PRCK at the Center for Nanophase Materials Sciences was sponsored at Oak Ridge National Laboratory by the Office of Basic Energy Sciences, DOE.

REFERENCES AND NOTES

1. Muller, C.; van Ruitenbeek, J. M.; de Jongh, L. J. Conductance and Supercurrent Discontinuities in Atomic-Scale Metallic Constrictions of Variable Width. *Phys. Rev. Lett.* **1992**, *69*, 140–143.
2. Krans, J. M.; van Rutlenbeek, J. M.; Fisun, V. V.; Yanson, I. K.; de Jongh, L. J. The Signature of Conductance Quantization in Metallic Point Contacts. *Nature* **1995**, *375*, 767–769.
3. Ohnishi, H.; Kondo, Y.; Takayanagi, K. Quantized Conductance through Individual Rows of Suspended Gold Atoms. *Nature* **1998**, *395*, 780–783.
4. Yanson, A. I.; Bollinger, G. R.; van den Brom, H. E.; Agrait, N.; van Ruitenbeek, J. M. Formation and Manipulation of a Metallic Wire of Single Gold Atoms. *Nature* **1998**, *395*, 783–785.
5. Guo, S.; Hihath, J.; Tao, N. Breakdown of Atomic-Sized Metallic Contacts Measured on Nanosecond Scale. *Nano Lett.* **2011**, *11*, 927–933.
6. Marszalek, P.; Greenleaf, W.; Li, H. Atomic Force Microscopy Captures Quantized Plastic Deformation in Gold Nanowires. *Proc. Natl. Acad. Sci. U.S.A.* **2000**, *97*, 6282–6286.
7. Coura, P.; Legoas, S.; Moreira, A.; Sato, F. On the Structural and Stability Features of Linear Atomic Suspended Chains Formed from Gold Nanowires Stretching. *Nano Lett.* **2004**, *4*, 1187–1191.
8. da Silva, E.; da Silva, A.; Fazzio, A. Breaking of Gold Nanowires. *Comput. Mater. Sci.* **2004**, *30*, 73–76.
9. Gall, K.; Diao, J.; Dunn, M. L. The Strength of Gold Nanowires. *Nano Lett.* **2004**, *4*, 2431–2436.
10. Sato, F.; Moreira, A. S.; Coura, P. Z.; Dantas, S. O.; Legoas, S. B.; Ugarte, D.; Galvão, D. S. Computer Simulations of Gold Nanowire Formation: The Role of Outlayer Atoms. *Appl. Phys. A* **2005**, *81*, 1527–1531.
11. Koh, S. J. A.; Lee, H. P. Molecular Dynamics Simulation of Size and Strain Rate Dependent Mechanical Response of FCC Metallic Nanowires. *Nanotechnology* **2006**, *17*, 3451–3467.
12. Pu, Q.; Leng, Y.; Tsetseris, L.; Park, H. S.; Pantelides, S. T.; Cummings, P. T. Molecular Dynamics Simulations of Stretched Gold Nanowires: The Relative Utility of Different Semiempirical Potentials. *J. Chem. Phys.* **2007**, *126*, 144707.
13. Wang, D.; Zhao, J.; Hu, S.; Yin, X.; Liang, S.; Liu, Y.; Deng, S. Where, and How, Does a Nanowire Break? *Nano Lett.* **2007**, *7*, 1208–1212.
14. Pu, Q.; Leng, Y.; Cummings, P. T. Rate-Dependent Energy Release Mechanism of Gold Nanowires under Elongation. *J. Am. Chem. Soc.* **2008**, *130*, 17907–17912.
15. Tsutsui, M.; Shoji, K.; Taniguchi, M.; Kawai, T. Formation and Self-Breaking Mechanism of Stable Atom-Sized Junctions. *Nano Lett.* **2008**, *8*, 345–349.
16. Lagos, M. J.; Sato, F.; Bettini, J.; Rodrigues, V.; Galvao, D. S.; Ugarte, D. Observation of the Smallest Metal Nanotube with a Square Cross-Section. *Nat. Nanotechnol.* **2009**, *4*, 149–152.
17. Tavazza, F.; Levine, L.; Chaka, A. Elongation and Breaking Mechanisms of Gold Nanowires under a Wide Range of Tensile Conditions. *J. Appl. Phys.* **2009**, *106*, 043522.
18. Barnett, R. N.; Landman, U. Cluster-Derived Structures and Conductance Fluctuations in Nanowires. *Nature* **1997**, *387*, 788–791.
19. Rego, L. G. C.; Rocha, A. R.; Rodrigues, V.; Ugarte, D. Role of Structural Evolution in the Quantum Conductance Behavior of Gold Nanowires during Stretching. *Phys. Rev. B* **2003**, *67*, 045412.
20. Lopez-Acevedo, O.; Koudela, D.; Häkkinen, H. Conductance through Atomic Point Contacts between fcc(100) Electrodes of Gold. *Eur. Phys. J. B* **2008**, *66*, 497–501.

21. Tavazza, F.; Smith, D. T.; Levine, L. E.; Pratt, J. R.; Chaka, A. M. Electron Transport in Gold Nanowires: Stable 1-, 2- and 3-Dimensional Atomic Structures and Noninteger Conduction States. *Phys. Rev. Lett.* **2011**, *107*, 126802.
22. French, W. R.; Iacovella, C. R.; Cummings, P. T. The Influence of Molecular Adsorption on Elongating Gold Nanowires. *J. Phys. Chem. C* **2011**, *115*, 18422–18433.
23. Fioravante, F.; Nunes, R. W. Semiconducting Chains of Gold and Silver. *Appl. Phys. Lett.* **2007**, *91*, 223115.
24. Park, H. S.; Cai, W.; Espinosa, H. D.; Huang, H. Mechanics of Crystalline Nanowires. *MRS Bull.* **2009**, *34*, 178–183.
25. Ikeda, H.; Qi, Y.; Çagin, T.; Samwer, K.; Johnson, W. L.; Goddard, W. A. Strain Rate Induced Amorphization in Metallic Nanowires. *Phys. Rev. Lett.* **1999**, *82*, 2900–2903.
26. Zhang, H.; Srolovitz, D. J.; Douglas, J. F.; Warren, J. A. Grain Boundaries Exhibit the Dynamics of Glass-Forming Liquids. *Proc. Natl. Acad. Sci. U.S.A.* **2009**, *106*, 7735–7740.
27. Velázquez-Salazar, J. J.; Esparza, R.; Mejía-Rosales, S. J.; Estrada-Salas, R.; Ponce, A.; Deepak, F. L.; Castro-Guerrero, C.; José-Yacamán, M. Experimental Evidence of Icosahedral and Decahedral Packing in One-Dimensional Nanostructures. *ACS Nano* **2011**, *5*, 6272–6278.
28. Jiang, D.-e.; Nobusada, K.; Luo, W.; Whetten, R. L. Thiolated Gold Nanowires: Metallic *versus* Semiconducting. *ACS Nano* **2009**, *3*, 2351–2357, PMID: 19603760.
29. Iacovella, C. R.; Keys, A. S.; Horsch, M. A.; Glotzer, S. C. Icosahedral Packing of Polymer-Tethered Nanospheres and Stabilization of the Gyroid Phase. *Phys. Rev. E* **2007**, *75*, 040801.
30. Keys, A. S.; Iacovella, C. R.; Glotzer, S. C. Characterizing Structure through Shape Matching and Applications to Self-Assembly. *Annu. Rev. Condens. Matter Phys.* **2011**, *2*, 263–285.
31. Keys, A. S.; Iacovella, C. R.; Glotzer, S. C. Characterizing Complex Particle Morphologies through Shape Matching: Descriptors, Applications, and Algorithms. *J. Comput. Phys.* **2011**, *230*, 6438–6463.
32. Häkkinen, H.; Barnett, R. N.; Scherbakov, A. G.; Landman, U. Nanowire Gold Chains: Formation Mechanisms and Conductance. *J. Phys. Chem. B* **2000**, *104*, 9063–9066.
33. Vélez, P.; Dassie, S. A.; Leiva, E. P. M. When Do Nanowires Break? A Model for the Theoretical Study of the Long-Term Stability of Monoatomic Nanowires. *Chem. Phys. Lett.* **2008**, *460*, 261–265.
34. Tavazza, F.; Levine, L. E.; Chaka, A. M. Structural Changes during the Formation of Gold Single-Atom Chains: Stability Criteria and Electronic Structure. *Phys. Rev. B* **2010**, *81*, 1–12.
35. Wu, H. Molecular Dynamics Study of the Mechanics of Metal Nanowires at Finite Temperature. *Eur. J. Mech. A* **2006**, *25*, 370–377.
36. Zhao, J.; Murakoshi, K.; Yin, X.; Kiguchi, M.; Y., G. Dynamic Characterization of the Postbreaking Behavior of a Nanowire. *J. Phys. Chem. C* **2008**, *112*, 20088–20094.
37. Xiao, L.; Wang, L. From Planar to Three-Dimensional Structural Transition in Gold Clusters and the Spin−Orbit Coupling Effect. *Chem. Phys. Lett.* **2004**, *392*, 452–455.
38. Keith, J. A.; Fantauzzi, D.; Jacob, T.; van Duin, A. C. T. Reactive Forcefield for Simulating Gold Surfaces and Nanoparticles. *Phys. Rev. B* **2010**, *81*, 235404.
39. Cleri, F.; Rosato, V. Tight-Binding Potentials for Transition Metals and Alloys. *Phys. Rev. B* **1993**, *48*, 22–33.
40. Gall, K.; Diao, J.; Dunn, M. L.; Haftel, M.; Bernstein, N.; Mehl, M. J. Tetragonal Phase Transformation in Gold Nanowires. *J. Eng. Mater. Technol.* **2005**, *127*, 417–422.
41. Järvi, T. T.; Kuronen, A.; Hakala, M.; Nordlund, K.; van Duin, A. C.; Goddard, W. A.; Jacob, T. Development of a ReaxFF Description for Gold. *Eur. Phys. J. B* **2008**, *66*, 75–79.
42. van Duin, A. C. T.; Dasgupta, S.; Lorant, F.; Goddard, W. A. ReaxFF: A Reactive Force Field for Hydrocarbons. *J. Phys. Chem. A* **2001**, *105*, 9396–9409.
43. Plimpton, S. J. Fast Parallel Algorithms for Short-Range Molecular Dynamic. *J. Comput. Phys.* **1995**, *117*, 1–19.
44. Frank, F.; Kasper, J. Complex Alloy Structures Regarded as Sphere Packings. I. Definitions and Basic Principles. *Acta Crystallogr.* **1958**, *11*, 184–190.
45. Iacovella, C. R.; Horsch, M. A.; Glotzer, S. C. Local Ordering of Polymer-Tethered Nanospheres and Nanorods and the Stabilization of the Double Gyroid Phase. *J. Chem. Phys.* **2008**, *129*, 044902.
46. Steinhardt, P. J.; Nelson, D. R.; Ronchetti, M. Bond-Orientational Order in Liquids and Glasses. *Phys. Rev. B* **1983**, *28*, 784–805.
47. Smithells, C. J., Ed. *Metal Reference Book*, 5th ed.; Butterworths: London, 1976.
48. Wang, B.; Yin, S.; Wang, G.; Buldum, A.; Zhao, J. Novel Structures and Properties of Gold Nanowires. *Phys. Rev. Lett.* **2001**, *86*, 2046–2049.
49. Driscoll, J. A.; Varga, K. Convergence in Quantum Transport Calculations: Localized Atomic Orbitals *versus* Nonlocalized Basis Sets. *Phys. Rev. B* **2010**, *81*, 115412.
50. Costa-Krämer, J. L. Conductance Quantization at Room Temperature in Magnetic and Nonmagnetic Metallic Nanowires. *Phys. Rev. B* **1997**, *55*, R4875–R4878.
51. Li, X.-B.; Wang, H.-Y.; Yang, X.-D.; Zhu, Z.-H.; Tang, Y.-J. Size Dependence of the Structures and Energetic and Electronic Properties of Gold Clusters. *J. Chem. Phys.* **2007**, *126*, 084505.
52. Gruber, M.; Heimel, G.; Romaner, L.; Brédas, J.-L.; Zojer, E. First-Principles Study of the Geometric and Electronic Structure of Au_{13} Clusters: Importance of the Prism Motif. *Phys. Rev. B* **2008**, *77*, 165411.
53. Pundlik, S. S.; Kalyanaraman, K.; Waghmare, U. V. First-Principles Investigation of the Atomic and Electronic Structure and Magnetic Moments in Gold Nanoclusters. *J. Phys. Chem. C* **2011**, *115*, 3809–3820.
54. Menard, L. D.; Xu, H.; Gao, S.-P.; Twesten, R. D.; Harper, A. S.; Song, Y.; Wang, G.; Douglas, A. D.; Yang, J. C.; Frenkel, A. I.; *et al.* Metal Core Bonding Motifs of Monodisperse Icosahedral Au13 and Larger Au Monolayer-Protected Clusters As Revealed by X-ray Absorption Spectroscopy and Transmission Electron Microscopy. *J. Phys. Chem. B* **2006**, *110*, 14564–14573.
55. Walter, M.; Akola, J.; Lopez-Acevedo, O. A Unified View of Ligand-Protected Gold Clusters as Superatom Complexes. *Proc. Natl. Acad. Sci. U.S.A.* **2008**, *105*, 9157–9162.
56. Pei, Y.; Gao, Y.; Zeng, X. C. Structural Prediction of Thiolate-Protected Au38: A Face-Fused Bi-icosahedral Au Core. *J. Am. Chem. Soc.* **2008**, *130*, 7830–7832.
57. Shichibu, Y.; Negishi, Y.; Watanabe, T.; Chaki, N. K.; Kawaguchi, H.; Tsukuda, T. Biicosahedral Gold Clusters $[Au_{25}(PPh_3)_{10}(SC_nH_{2n+1})_5Cl_2]^{2+}$ (n = 2−18): A Stepping Stone to Cluster-Assembled Materials. *J. Phys. Chem. C* **2007**, *111*, 7845–7847.
58. Agrait, N.; Rubio, G.; Vieira, S. Plastic Deformation of Nanometer-Scale Gold Connective Necks. *Phys. Rev. Lett.* **1995**, *74*, 3995–3998.
59. Zheng, C.; Hoffmann, R.; Nelson, D. R. A Helical Face-Sharing Tetrahedron Chain from Irrational Twist, Stella Quadrangula, and Related Matters. *J. Am. Chem. Soc.* **1990**, *112*, 3784–3791.
60. Lidin, S.; Andersson, S. Regular Polyhedra Helices. *Z. Anorg. Allg. Chem.* **1996**, *622*, 164–166.
61. Vetter, J.; Glassbrook, R.; Dongarra, J.; Schwan, K.; Loftis, B.; McNally, S.; Meredith, J.; Rogers, J.; Roth, P.; Spafford, K.; *et al.* Keeneland: Bringing Heterogeneous GPU Computing to the Computational Science Community. *IEEE Comput. Sci. Eng.* **2011**, *13*, 90–95.
62. Perdew, J. P.; Burke, K.; Ernzerhof, M. Generalized Gradient Approximation Made Simple. *Phys. Rev. Lett.* **1996**, *77*, 3865.
63. Kresse, G.; Furthmuller, J. Efficient Iterative Schemes for *Ab Initio* Total-Energy Calculations Using a Plane-Wave Basis Set. *Phys. Rev. B* **1996**, *54*, 11169.
64. Kresse, G.; Joubert, D. From Ultrasoft Pseudopotentials to the Projector Augmented-Wave Method. *Phys. Rev. B* **1999**, *59*, 1758.